

Article

Large-Scale Consumption and Zero-Waste Recycling Method of Red Mud in Steel Making Process

Guoshan Ning^{1,2}, Bo Zhang^{1,2,*}, Chengjun Liu^{1,2}, Shuai Li^{1,2}, Yun Ye^{1,2} and Maofa Jiang^{1,2}

¹ School of Metallurgy, Northeastern University, Shenyang 110819, China; ninggs_neu@163.com (G.N.); liucj@smm.neu.edu.cn (C.L.); lis_neu@163.com (S.L.); 20152529@stu.neu.edu.cn (Y.Y.); jiangmf@smm.neu.edu.cn (M.J.)

² Key Laboratory for Ecological Metallurgy of Multimetallic Ores (Ministry of Education), Northeastern University, Shenyang 110819, China

* Correspondence: zhangbo@smm.neu.edu.cn

Received: 14 February 2018; Accepted: 1 March 2018; Published: 6 March 2018

Abstract: To release the environmental pressure from the massive discharge of bauxite residue (red mud), a novel recycling method of red mud in steel making process was investigated through high-temperature experiments and thermodynamic analysis. The results showed that after the reduction roasting of the carbon-bearing red mud pellets at 1100–1200 °C for 12–20 min, the metallic pellets were obtained with the metallization ratio of $\geq 88\%$. Then, the separation of slag and iron achieved from the metallic pellets at 1550 °C, after composition adjustment targeting the primary crystal region of the $12\text{CaO}\cdot 7\text{Al}_2\text{O}_3$ phase. After iron removal and composition adjustment, the smelting-separation slag had good smelting performance and desulfurization capability, which meets the demand of sulfurization flux in steel making process. The pig iron quality meets the requirements of the high-quality raw material for steel making. In virtue of the huge scale and output of steel industry, the large-scale consumption and zero-waste recycling method of red mud was proposed, which comprised of the carbon-bearing red mud pellets roasting in the rotary hearth furnace and smelting separation in the electric arc furnace after composition adjustment.

Keywords: red mud; reduction roasting; smelting separation; pig iron; desulfurization flux; sulfur capacity

1. Introduction

Red mud is a product term that refers to the industrial solid waste discharged during the Al_2O_3 production from bauxite. The most commonly utilized method for Al_2O_3 production is the Bayer process, in which NaOH is used to dissolve bauxite. Also, the slurry sludge that is separated after dissolution is the red mud. Each year, approximately 140 million tons of red mud is generated worldwide [1]. By the end of 2015, the stock of red mud exceeded 2.7×10^9 tons [2]. The stacking of red mud occupies a substantial amount of land and consumes increased amounts of construction and maintenance costs of a yard. The alkali in the red mud infiltrates the ground and results in groundwater and soil contaminations. The dust formed by the naked red mud is dispersed in the wind and pollutes the atmosphere, which causes negative impacts on the survival of humans, animals and plants, polluting the ecological environment. Due to the dike breach of a red mud stockpiling yard, between 600,000 and 700,000 m^3 of red mud was released at the Ajkai Timfoldgyar Zrt alumina plant in Hungary on 4 October 2010, which caused serious environmental pollution [3]. Therefore, it is indispensable and quite urgent to promote the detoxification and reduction treatment for red mud. At the same time, the red mud contains a certain amount of Fe, Al, Si, as well as low amounts of rare metal elements, consequently displaying a recycling value. Currently, the integrated utilized approach and method for red mud are mainly focused on the production of building materials [4–6],

the application in environmental protection [7–9], the application in industrial catalysts [10], the soil amendment and the extraction of valuable metal elements [11–14]. Although there are many kinds of recycling methods of red mud, the treatment capacity is still limited relative to the huge discharged amount of red mud. Therefore, a lack for a processing approach still exists, with which, high amounts of red mud could be utilized and have industrial competitiveness.

In general, the iron oxide accounts for over 60 wt % of the red mud produced by the Bayer process. The reduction roasting technology utilization for red mud processing can accomplish the recycling and utilization of iron resources but the residuals still cause severe environmental pressure [15]. Following the removal of iron, the main components of red mud are SiO_2 , Al_2O_3 and a low amount of CaO , with a composition similar to the calcium aluminate-refining slag, used in steel making as desulfurization flux. If the red mud following the iron removal is processed into the desulfurization flux used in steel making, the zero-waste target of red mud disposal could be reached. In 2017, the global production of crude steel exceeded 1.6 billion tons. Generally speaking, the consumption of desulfurization flux per ton of steel was approximately 5~15 kg [16,17], indicating that the steel industry has a huge demand for desulfurization fluxes. If the recycling of iron from red mud and the application of red mud in desulfurization are simultaneously achieved, the large-scale consumption of red mud and the high-value added utilization of red mud are expected to be accomplished.

In the present paper, the combined process of carbon-bearing pellet roasting (pre-reduction) and the smelting separation (final reduction) was studied through high-temperature simulated experiments; the desulfurization capability of the smelting-separation slag after iron removal and composition adjustment was evaluated through the calculations of the melting point and sulfur capability. Furthermore, the large-scale consumption and zero-waste recycling method of red mud was proposed.

2. Experimental

2.1. Roasting of the Carbon-Bearing Pellets (Pre-Reduction)

Table 1 shows the composition of the red mud, which was supplied by the CHALCO Shandong Co., LTD (Zibo, China) and produced by the Bayer process. Table 2 shows the composition of the semi-coke used as reductant, which was produced from the Shenfu coal field in Yulin, China. The chemical compositions were analyzed by X-ray Fluorescence Spectrometer (XRF) (Rigaku Corporation, Tokyo, Japan) and chemical analysis. The pressure-forming pellets were prepared by adding some water (0.4–0.6 mL) into the uniform mixed powders (8.50 g), which were comprised of red mud powders (6.83 g) and semi-coke powders (1.67 g) with the particle size of <0.074 mm and pressing at the pressure of 30 MPa in a mold. Then, the pellets were heated at 110 °C for four hours. Considering the reduction reaction of the iron oxides and carburization of the iron product, the molar ratio of carbon and oxygen (only in iron oxides) in the pellets is 1.2:1.

Table 1. Chemical composition of the red mud (mass%).

Fe_2O_3	TiO_2	Na_2O	K_2O	CaO	SiO_2	Al_2O_3	MgO	LOI
67.01	3.92	1.725	0.078	0.35	5.01	7.90	0.09	13.24

Table 2. Chemical composition of the semi-coke (mass%).

C	Volatile	Ash	H_2O
74.26	11.53	9.98	4.23

The reduction roasting experiments were carried out in a vertical tube furnace shown in Figure 1. When the temperature of the heating zone in the furnace reached at an appointed temperature (900 °C,

1000 °C, 1100 °C, 1200 °C, 1300 °C), argon gas swept through the bottom of the furnace with a flow rate of $1 \text{ L}\cdot\text{min}^{-1}$. Then, the molybdenum basket loading of 5 pellets hung under the electronic balance with the accuracy of $\pm 0.1 \text{ mg}$ and the weight data acquisition program simultaneously launched by the computer with a time interval of 30 s. After the weight data maintained at a steady value for 300 s, the molybdenum basket was taken out and the pellets cooled by blowing with argon gas. The content of total Fe and metallic Fe in the pellets was determined using the potassium dichromate volumetric method according to the Chinese standard (GB/T6730.5-2007) and the content of carbon in the pellets was determined using infrared absorption method.

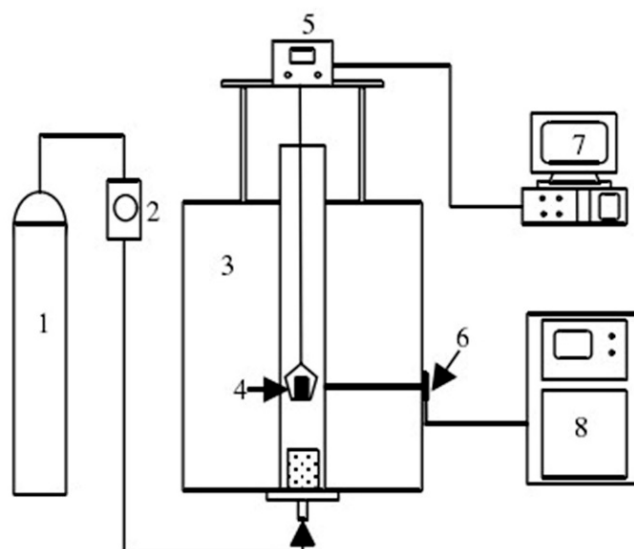


Figure 1. Schematic diagram of the reduction roasting experimental apparatus (1—argon cylinder; 2—flowmeter; 3—furnace; 4—molybdenum basket; 5—electronic balance; 6—Thermocouple; 7—data logging device; 8—temperature control device).

2.2. Smelting Separation (Final Reduction)

Following the iron oxides reduction in red mud, the melting point of the slag system formed by the residual oxides is the key factor determining the smelting separation performance of the slag-iron system. In this study, the $\text{CaO-SiO}_2\text{-Al}_2\text{O}_3$ phase diagram [18] was selected as the basis for the slag system composition adjustment in the smelting separation. The positions of the circle in Figure 2 corresponded to the positions of CaO, SiO_2 and Al_2O_3 components in the red mud following iron removal, while the corresponding composition of the dotted line could be obtained simply through the CaO content adjustment. Among these positions, the No. 1 square position had a low melting point and was selected for the composition adjustment; the No. 4 square position was located in the primary crystal region of the $12\text{CaO}\cdot 7\text{Al}_2\text{O}_3$ phase with a low melting point, while the No. 2, 3 and 5 square positions were located around the primary crystal region of $12\text{CaO}\cdot 7\text{Al}_2\text{O}_3$, all of which had low melting points. The slag compositions of Nos. 1~5 that are listed in Table 3 were selected as the targets for the composition adjustment of the metallized pellets obtained during pre-reduction. The smelting separation (final reduction) experiments were carried out for the metallized pellets after composition adjustment.

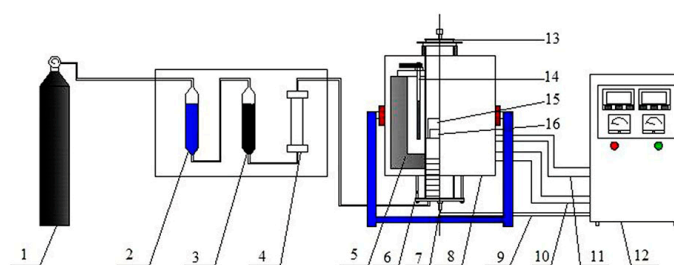


Figure 3. Schematic diagram of smelting separation experimental apparatus (1—argon cylinder; 2—silica gel; 3—molecular sieve; 4—flowmeter; 5—refractory brick; 6—alumina furnace tube; 7—thermocouple I; 8—furnace body; 9—thermocouple compensation wire; 10—power wires; 11—thermocouple II and compensation wire; 12—temperature control device 13—furnace lid; 14—MoSi₂ heating element; 15—protective crucible; 16—graphite crucible).

3. Results and Discussion

3.1. Pre-Reduction of Iron Oxides in Red Mud

Figure 4 presents the XRD pattern of the red mud. The XRD analysis result indicated that the red mud phase is mainly composed of α -goethite (α -FeO(OH)), hematite (Fe₂O₃) and bauxite (Al₂O₃·xH₂O). In addition, high amounts of non-crystalline minerals existed.

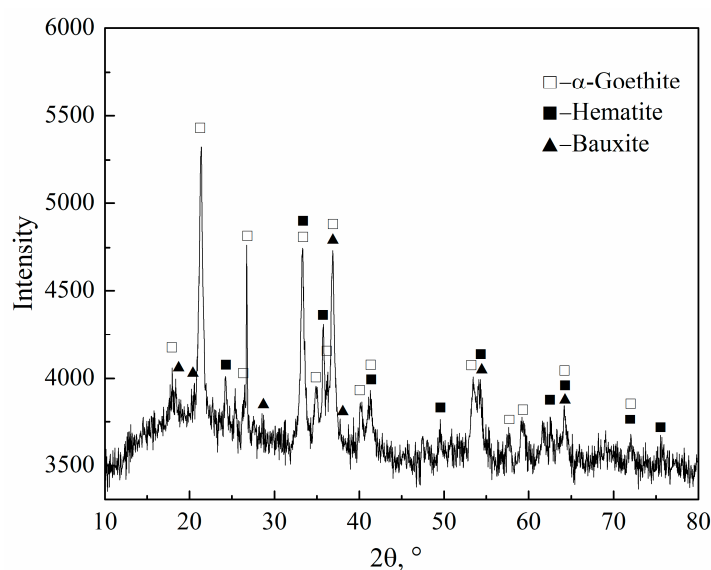
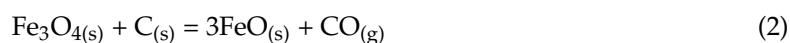
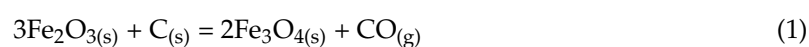
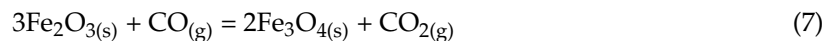
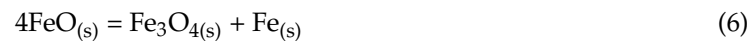


Figure 4. XRD analysis of the red mud.

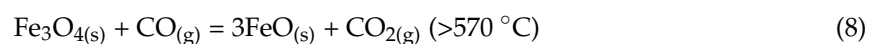
The reduction roasting of iron oxides in red mud follows a stepwise principle. As it could be observed from Equations (1)–(4), the iron oxides could be converted into metallic iron, according to the sequence of Fe₂O₃→Fe₃O₄→FeO→Fe. Subsequently, the metallic iron could be converted into Fe₃C through a further carburizing reaction.



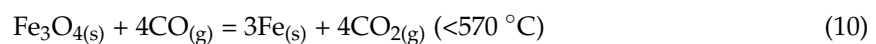
When the Boudouard reaction, as presented in Equation (5), occurs intensively, the reductant that is in direct contacts with the iron oxide changes to CO [19]. When the temperature is below 570 °C, the FeO has a decomposition reaction as presented in Equation (6). Therefore, the CO reduction sequence for iron oxides is $\text{Fe}_2\text{O}_3 \rightarrow \text{Fe}_3\text{O}_4 \rightarrow \text{FeO} \rightarrow \text{Fe}$ at temperatures above 570 °C as shown in Equations (7)–(9), while the sequence changes to $\text{Fe}_2\text{O}_3 \rightarrow \text{Fe}_3\text{O}_4 \rightarrow \text{Fe}$ when the temperature is below 570 °C as shown in Equations (7) and (10).



When above 570 °C,



When below 570 °C,



Based on the weight-loss method, the reaction fraction, f , which represent the reduction degree of iron oxides can be calculated using Equation (11) [20]. The relationship between the reduction degree and time during the roasting of carbon-bearing red mud pellets was measured through thermogravimetry experiment and is presented in Figure 5. It could be observed from Figure 5 that the effect of temperature on reduction was significant. The reduction extent increased as both the temperature and reaction time increased. Also, the reduction was accelerated as the temperature increased.

$$f = \frac{\Delta W_t}{\Delta W_{\text{max}}} = \frac{(W_0 - W_t)}{W_0 \cdot \frac{M_{\text{CO}}}{M_{\text{O}}}} \times 100\% \quad (11)$$

where f is the reaction fraction, ΔW_t is the weight loss at the time of t (g), ΔW_{max} is the maximum theoretical reduction weight loss (g), W_0 is the initial weight of the pellets (g), W_t is the weight of the pellets at the time of t (g), W_{O} is the oxygen weight of the iron oxides in the pellets (g), M_{CO} is the molar mass of the carbon monoxide ($\text{g}\cdot\text{mol}^{-1}$), M_{O} is the molar mass of the oxygen ($\text{g}\cdot\text{mol}^{-1}$).

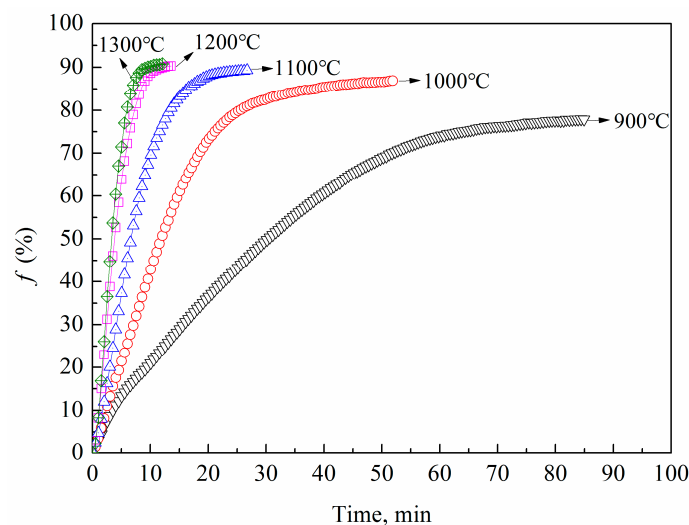


Figure 5. Variation of reaction fraction at different times in the roasting process.

The effects of roasting temperature on the metallization ratio of pellets and the residual carbon content in pellets are presented in Figure 6. In the temperature range of 900–1200 °C, as the roasting temperature increased, the metallization ratio of the pellets increased. The main reason was that the reduction reaction of iron oxides was an endothermic reaction. Consequently, the higher temperature shifted the reaction to its positive direction. In addition, the temperature increase could promote the gasification reaction of carbon (Boudouard reaction) and the aggregation of metallic iron. If the temperature increased beyond 1200 °C, the metallization ratio of pellets did not apparently vary and it increased by only 0.7%. The reason was that, under high temperature, the FeO reduced from the iron oxides in the red mud was easy to react with SiO₂, consequently forming fayalite (2FeO·SiO₂). The reactions are presented as Equations (12). The fayalite exhibited a liquid phase under high temperature due to its melting point of 1205 °C and the liquid phase trapped portions of red mud and carbon particles. The entrapment prevented the contact between the solid phases or the contact between the gas and solid phases, leading to lower surface area of contact, which resulted in a barrier formation, inhibiting the metallization ratio increase. In addition, the liquid phase filled the pores inside the pellets and increased the diffusion resistance for both CO and CO₂, which deteriorated the kinetic conditions of reduction.



With regards to the aforementioned analysis, the optimal temperature range for reduction roasting was 1100–1200 °C. After reduction for 12–20 min under these temperatures, the metallization ratio of carbon-bearing red mud pellets could reach up to 88%, demonstrating a good reduction.

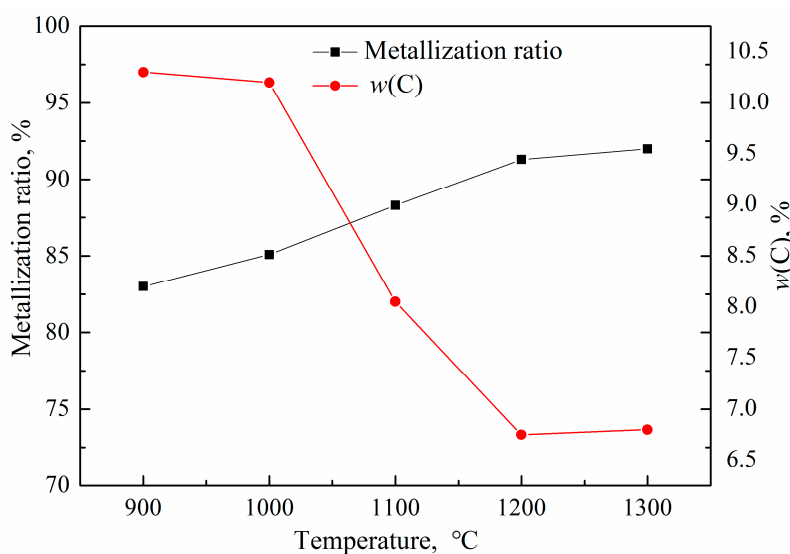


Figure 6. Effect of roasting temperature on metallization ratio and residual carbon.

3.2. Smelting Separation and Final Reduction Following Composition Adjustment

Figure 7 presents the materials inside the crucible after high-temperature smelting separation. The No. 1 experimental sample did not achieve the separation of slag and iron and a high amount of slag particles were adhered on the crucible wall. The morphology indicated that a severe foaming phenomenon of slag occurred at 1550 °C and a portion of slag was spilt over the crucible, along with particles of metallic iron. As presented in the No. 3 experimental sample morphology, the milky white material was slag and the iron droplets settled down and aggregated into iron beads, indicating a better separation of slag and iron. Following smelting separation, the phase composition of iron is presented in Table 4. According to the Chinese National Standard of GB/T717-1998, the composition of pig iron was in agreement with the “L04” level, consequently belonging to the high-quality raw

material for steel making. Figure 8 presents the recovery of iron in the metallic phase during the smelting separation of No. 2–No. 5 samples. Except the lower iron recovery (72.5%) of No. 2 sample, all the recoveries of No. 3, No. 4 and No. 5 samples were beyond 92%.

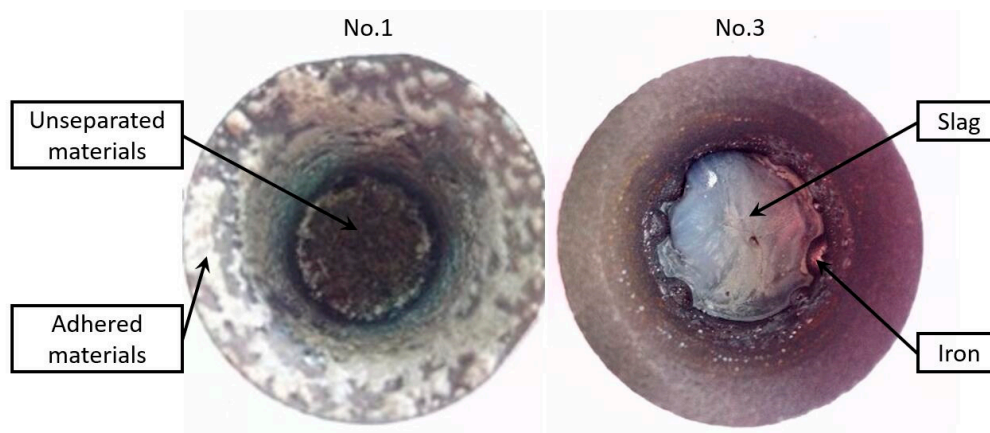


Figure 7. Picture of materials inside the crucible after smelting separation.

Table 4. Composition of the metallic phase after smelting separation (mass%).

Experiment No.	C	S	P	Si
2	5.73	0.012	0.19	0.012
3	5.34	0.016	0.16	0.013
4	4.87	0.007	0.44	0.021
5	5.79	0.012	0.24	0.012

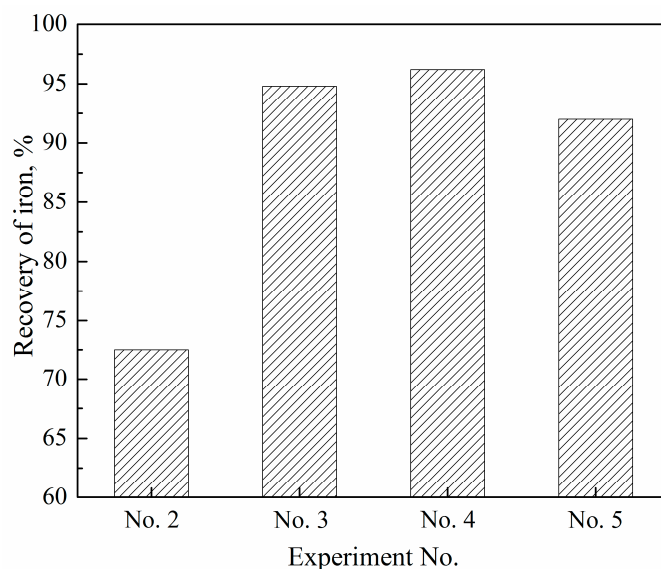


Figure 8. Recovery of iron in the metallic phase after smelting separation.

The smelting separation of metallized pellets included two basic physical processes: the smelting of metallized pellets and the slag-metal interface formation. The final reduction of iron oxides accompanied these two physical processes. Consequently, the entire smelting separation could be described as follows:

- (a) Metallized pellets began to smelt when the melting temperature was reached;

- (b) As the temperature increased further, the crystalline grains of metallic iron aggregated and grew. The iron began to settle down at the bottom of the graphite crucible, forming liquid iron and becoming separated from the slag, indicating the slag-metal interface formation.
- (c) The residual iron oxides in the slag at the slag-metal interface could have interfacial chemical reactions with [C] in the liquid iron. The generated gas could float inside the smelting-separation slag and discharge the slag. The newly-formed droplets of liquid iron settled down underneath the slag-metal interface.

The composition of smelting-separation slag is presented in Table 5. It could be observed from the composition that the contents of T.Fe in the smelting-separation slag were below 0.5%, indicating the good reduction and separation performance for slag and iron. Also, the phosphorus and sulfur contents in the slag were low.

Table 5. Chemical composition of the slag after smelting separation (mass %).

Experiment No.	T.Fe *	CaO	Al ₂ O ₃	SiO ₂	TiO ₂	MgO	Na ₂ O	K ₂ O	S	p
2	0.48	44.38	35.32	9.23	6.82	0.17	2.97	0.12	0.189	<0.005
3	0.14	53.89	35.74	4.57	3.62	0.08	1.41	0.06	0.095	0.006
4	0.11	48.31	41.21	4.71	3.47	0.08	1.55	0.07	0.100	<0.005
5	0.15	43.71	46.03	4.68	3.33	0.07	1.45	0.07	0.088	<0.005

* T.Fe is the total concentration of iron (element) in the red mud.

Figure 9 presents the XRD analysis results of the smelting-separation slag. The XRD analysis results demonstrated that the main phase in the No. 1 experimental slag was $2\text{CaO}\cdot\text{Al}_2\text{O}_3\cdot\text{SiO}_2$, along with the incompletely reduced FeO and ilmenite, formed by the reaction between FeO and TiO₂. In the No. 2 experimental slag, the FeO and FeO·TiO₂ disappeared and the main phases were two phases with high melting points: $2\text{CaO}\cdot\text{Al}_2\text{O}_3\cdot\text{SiO}_2$ and CaO·TiO₂. The main phases in the No. 3 and No. 4 experimental slags were $12\text{CaO}\cdot 7\text{Al}_2\text{O}_3$ and CaO·TiO₂, while the former $12\text{CaO}\cdot 7\text{Al}_2\text{O}_3$ with a low melting temperature was dominant. Besides the $12\text{CaO}\cdot 7\text{Al}_2\text{O}_3$ and CaO·TiO₂ phases existence, the CaO·Al₂O₃ phase with a relatively higher melting point existed.

Figure 10 presents the isothermal liquidus curves of the CaO-Al₂O₃-SiO₂-6.8 mass% TiO₂-3.0 mass% Na₂O slag system and CaO-Al₂O₃-SiO₂-3.5 mass% TiO₂-1.5 mass% Na₂O slag system. These isothermal liquidus curves were calculated with the FactSage software (version 7.1) [21]. It could be observed from Figure 10 that the No. 1 experimental slag melting point was approximately 1500 °C and the experimental temperature was 1550 °C. Therefore, the degree of superheat was only 50 °C. The lower degree of superheat resulted in higher viscosity and poorer fluidity of the slag, which was unfavorable to the smelting reduction reaction as well as to the separation of slag and iron, consequently leading to unreduced FeO and FeO·TiO₂ existing in the slag as shown in Figure 9. The presence of $2\text{CaO}\cdot\text{Al}_2\text{O}_3\cdot\text{SiO}_2$ in the No. 2 experimental slag and CaO·Al₂O₃ in No. 5 experimental slag led to the higher melting points (1400–1500 °C) compared to the No. 3 and No. 4 experimental slags (1300–1400 °C). Correspondingly, the iron recovery of the No. 2 and No. 5 experimental systems was also lower compared to the No. 3 and No. 4 experimental systems. The results indicated that the melting point of the slag system directly affected the separation effect between the slag and the iron. In the gray areas of Figure 10, the melting points of the slag systems were below 1400 °C. It could be inferred that a better separation effect between slag and iron could be achieved through the smelting-separation slag composition adjustment within the dark area.

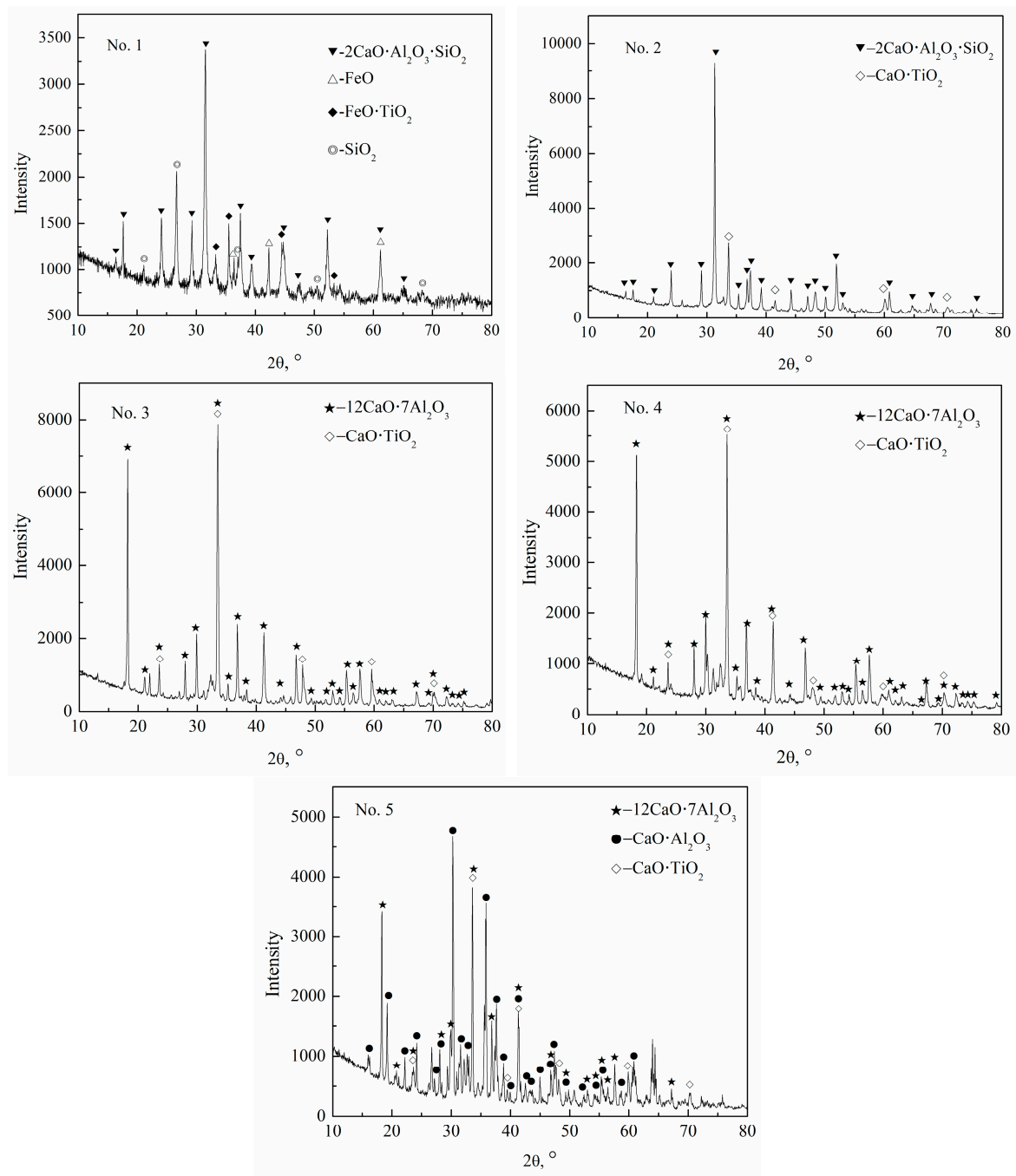
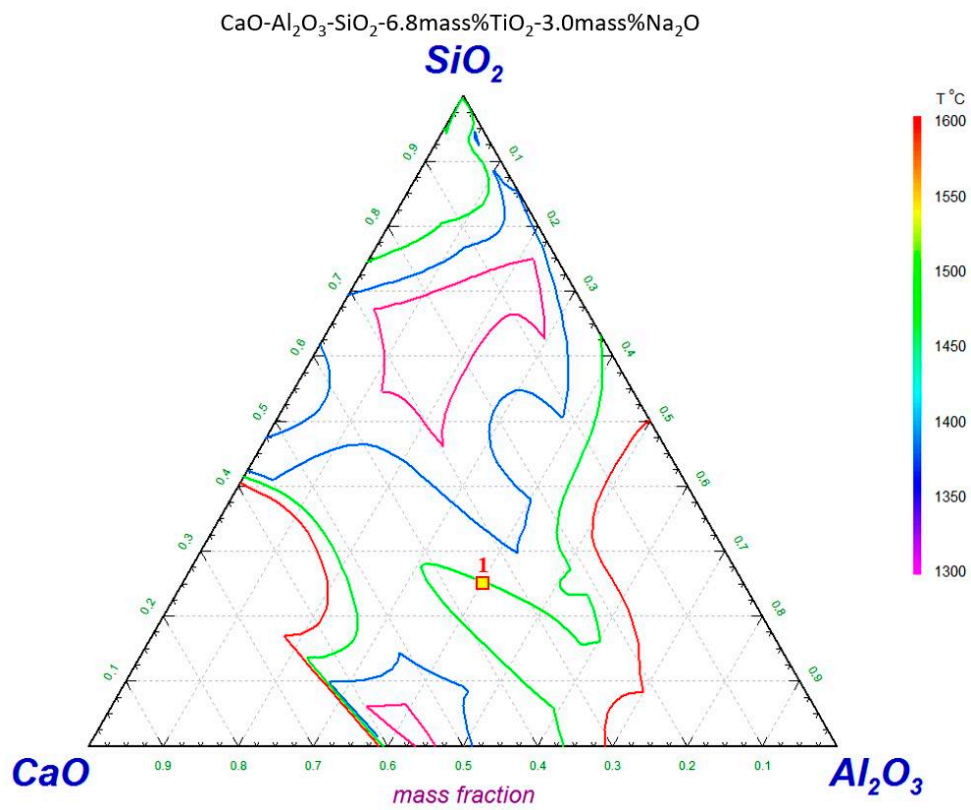
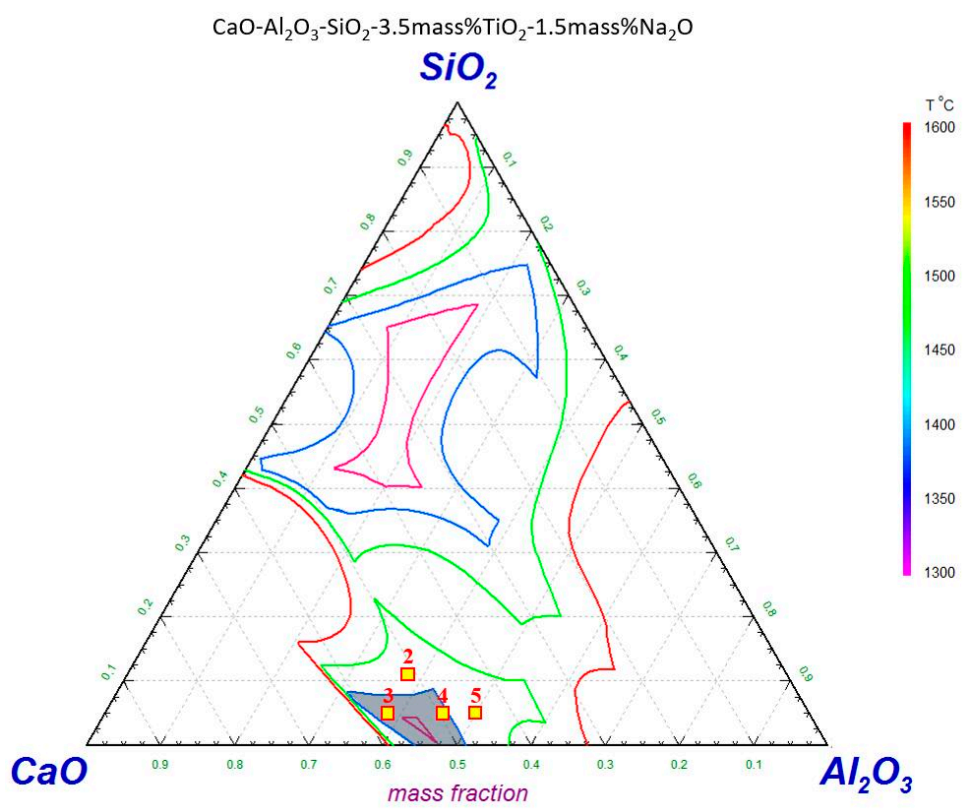


Figure 9. XRD analysis of the smelting separation slags including No. 1 slag, No. 2 slag, No. 3 slag, No. 4 slag, and No. 5 slag.



(a)



(b)

Figure 10. Isothermal liquidus curves of the CaO-Al₂O₃-SiO₂-6.8 mass% TiO₂-3.0 mass% Na₂O slag system (a) and CaO-Al₂O₃-SiO₂-3.5 mass% TiO₂-1.5 mass% Na₂O slag system (b).

3.3. Sulfur Capacity of Smelting-Separation Slag

In the following section, the desulfurization performance of smelting-separation slag was evaluated through the sulfur capacity (C_S) calculation.

Duffy et al. proposed the equation for the mean optical basicity calculation of a multi-component slag, as presented in Equations (13) and (14) [22].

$$\Lambda = \sum_{i=1}^n X_i^{O^{2-}} \cdot \Lambda_i \quad (13)$$

$$X_i^{O^{2-}} = \frac{O_i \cdot X_i}{\sum_{i=1}^n O_i \cdot X_i} \quad (14)$$

where Λ is the mean optical basicity of the slag; Λ_i is the optical basicity of component i , i represents the component in the slag; $X_i^{O^{2-}}$ is the molar fraction of oxygen ion of component i in the slag; O_i is the molar number of oxygen ion in component i ; X_i is the molar fraction of component i in the slag.

Table 6 presents the optical basicity of oxides in red mud. The desulfurization capability of slag is related to its optical basicity. The mean optical basicity of the smelting-separation slag was calculated through Equations (13) and (14), while the results are presented in Table 7.

Table 6. Optical basicity of the oxides in red mud.

Compound	Λ	Compound	Λ
CaO	1.00	FeO	0.51
Al ₂ O ₃	0.61	Fe ₂ O ₃	0.48
MgO	0.78	Na ₂ O	1.15
SiO ₂	0.48	K ₂ O	1.40
TiO ₂	0.61	P ₂ O ₅	0.40

Table 7. Average optical basicity of the smelting separation slag.

Slag No.	2	3	4	5
Λ	0.735	0.771	0.751	0.734

According to the data calculation results listed in Table 7, the optical basicity range of the smelting-separation slag was 0.73–0.78. When $\Lambda < 0.8$, the relationship between C_S and Λ can be presented in Equation (15) [23].

$$\lg C_S = -13.913 + 42.84\Lambda - 23.82\Lambda^2 - \frac{11710}{T} - 0.02223(\%SiO_2) - 0.02275(\%Al_2O_3) \quad (15)$$

where T is the temperature, K; ($\%SiO_2$) is the mass fraction of SiO₂ in the slag, %; ($\%Al_2O_3$) is the mass fraction of Al₂O₃ in the slag, %.

With the liquid steel composition consideration, as listed in Table 8, as the representative of molten steel, the sulfur ratio (L_S) between slag and molten steel at 1600 °C was calculated based on Equation (16) [24].

$$\lg L_S = \lg \frac{(\%S)}{[\%S]} = \lg C_S - \frac{935}{T} + 1.375 + \lg f_S - \lg a_{[O]} \quad (16)$$

where T is the temperature, K; ($\%S$) is the mass fraction of sulfur in the slag, %; [$\%S$] is the mass fraction of sulfur in the molten steel, %; f_S is the activity coefficient of sulfur in the molten steel; $a_{[O]}$ is the activity of oxygen in the molten steel.

Table 8. Chemical composition of molten steel (mass%).

C	Si	Mn	Al	P	S	V
0.34	0.27	1.6	0.01	0.003	0.005	0.0063

The activity interaction coefficients of the elements in the molten steel were calculated through the Wagner equation, as presented in Equation (17) and the activities of the elements in the molten steel were calculated through Equation (18). The activity interaction coefficients between sulfur or aluminum and other elements in molten steel are listed in Table 9.

$$\log f_i = \sum \left(e_i^j \cdot [\%j] \right) \quad (17)$$

$$a_{[i]} = f_i \cdot [\%i] \quad (18)$$

where f_i is the activity coefficient of element i in the molten steel, i represents the dissolved element in the molten steel; e_i^j represents the interaction coefficient of j to i ; $[\%j]$ is the mass fraction of element j in the molten steel, %; $a_{[i]}$ is the activity of element i in the molten steel.

Table 9. Activity interaction coefficients in molten steel.

Element (j)	C	Si	Mn	Al	P	S	V
e_S^j	0.11	0.063	−0.026	0.035	0.029	−0.028	−0.016
e_{Al}^j	0.091	0.056	-	0.045	-	0.03	-

The $a_{[O]}$ was calculated through the reaction between dissolved aluminum and oxygen in molten steel shown as Equation (19).



$$\Delta G^\theta = -1226832 + 390.66T \text{ (J}\cdot\text{mol}^{-1}) \quad (20)$$

$$\Delta G = \Delta G^\theta + RT \ln K \quad (21)$$

where ΔG^θ is the standard Gibbs free energy change of Equation (19); ΔG is the actual Gibbs free energy change of Equation (19); T is the thermodynamic temperature, K; R is the universal gas constant; K is the equilibrium constant, which can be expressed in Equation (22) when ΔG is zero.

$$K = \exp\left(-\frac{\Delta G^\theta}{RT}\right) = \frac{a_{(Al_2O_3)}}{a_{[Al]}^2 \cdot a_{[O]}^3} \quad (22)$$

where $a_{(Al_2O_3)}$ is the activity of Al_2O_3 in the slag; $a_{[Al]}$ is the activity of dissolved aluminum in the molten steel, which was calculated through Equations (17) and (18). At 1600 °C, the activity of Al_2O_3 in the slag can be expressed through Equation (23) [25].

$$\log a_{Al_2O_3} = \frac{-0.275(\%CaO) + 0.167(\%MgO)}{(\%SiO_2)} + 0.033(\%Al_2O_3) - 1.560 \quad (23)$$

where $(\%CaO)$ is the mass fraction of CaO in the slag, %; $(\%MgO)$ is the mass fraction of MgO in the slag, %; $(\%SiO_2)$ is the mass fraction of SiO_2 in the slag, %; $(\%Al_2O_3)$ is the mass fraction of Al_2O_3 in the slag, %.

Finally, $a_{[O]}$ was calculated through Equation (22) and then substituted into Equation (16). The sulfur capacity of smelting-separation slag (C_S) and the equilibrium distribution ratio (L_S) of sulfur between slag and molten steel at 1600 °C can be obtained. The calculated results are presented in Table 10.

The calculation results in Table 10 indicated that the $\lg C_S$ range of smelting-separation slag was -2.71 to -2.21 . It was reported that the $\lg C_S$ range of the $\text{CaO-SiO}_2\text{-CaF}_2$ slag system was -4.0 to -2.0 and the $\lg C_S$ range of the $\text{CaO-Al}_2\text{O}_3\text{-SiO}_2\text{-CaF}_2$ slag system was -3.5 to -2.5 [26]. The above-mentioned two slag systems are the classic desulfurization flux used in the refining process of steel making. The comparison indicated that the smelting-separation slag had a higher sulfur capacity than the classic desulfurization flux. By comparing the calculation results listed in Table 10, the No. 3 and No. 4 experimental slags had higher sulfur capacities, with the corresponding distribution ratios of sulfur between slag and iron reaching up to 1086.27 and 372.81, which are sufficient for desulfurization of steel making, respectively.

Table 10. Calculation results of the sulfur capacity and the equilibrium distribution ratio of sulfur between slag and molten steel at 1600 °C.

Slag No.	$\lg C_S$	C_S	L_S
2	-2.555	0.0027	112.93
3	-2.208	0.0062	1086.27
4	-2.472	0.0034	372.81
5	-2.707	0.0020	158.31

3.4. Process Flow

It could be inferred that after the composition adjustment of metallic pellets, according to the gray area in Figure 10, the smelting-separation slag had a lower melting point, an improved fluidity, an improved separation effect and a higher sulfur capacity. Therefore, a zero-waste process for recycling red mud could be proposed, as presented in Figure 11. During this flow, the pig iron and desulfurization flux used in steel making process were prepared through the combined process of the carbon-bearing red mud pellets roasting and smelting separation after composition adjustment. The new process could be carried out with a rotary hearth furnace for reduction roasting. Then, the reduced pellets could be directly thermally-loaded into an electric arc furnace for composition adjustment and smelting separation. The pig iron quality obtained could meet the requirements of steel making and the slag could have good smelting performance and desulfurization capability. The process combines the alumina and steel industries techniques, which could not only solve the problem of red mud processing in the alumina plant but also assist the iron and steel enterprises to reduce their production cost and improve their market competitiveness. The steel industry has a huge scale and output; therefore, the recycling of red mud in steel making process would significantly consume red mud along with its utilization and have a wide range of prospects.

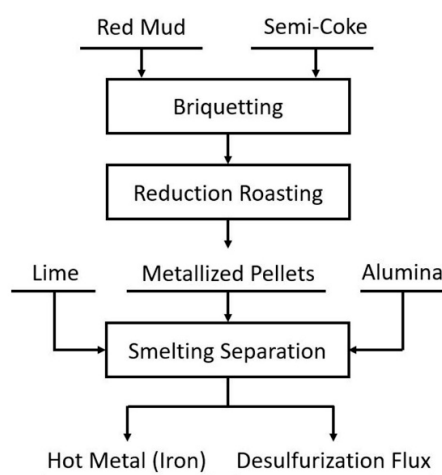


Figure 11. A new process for recycling of red mud.

4. Conclusions

In this study, a novel recycling method of bauxite residue (red mud) was investigated through high-temperature experiments and thermodynamic analysis. The results are shown as follows.

- (1) After the reduction roasting of the carbon-bearing red mud pellets at 1100–1200 °C for 12–20 min, the metallization ratio of pellets reached up to 88%.
- (2) After composition adjustment targeting the primary crystal region of the $12\text{CaO}\cdot 7\text{Al}_2\text{O}_3$ phase, the separation of slag and iron achieved from the metallic pellets at 1550 °C. The pig iron quality obtained could meet the requirements of the high-quality raw material for steel making and the recovery of iron was beyond 92%.
- (3) After iron removal and composition adjustment within the optimized composition zone in the $\text{CaO-Al}_2\text{O}_3\text{-SiO}_2\text{-TiO}_2\text{-Na}_2\text{O}$ slag system, the smelting-separation slag had the low melting point (≤ 1400 °C) and the high desulfurization capability, which meets the demand of desulfurization flux in steel making process.
- (4) In virtue of the huge scale and output of steel industry, the large-scale consumption and zero-waste recycling method of red mud was proposed, which comprised of the carbon-bearing red mud pellets roasting in the rotary hearth furnace and smelting separation in the electric arc furnace after composition adjustment.

Acknowledgments: Financial support to this project is provided by the National Key R & D Program of China (Grant No. 2017YFC0805100), the National Natural Science Foundation of China (Grant No. 51774087), the Fundamental Research Funds for the Central Universities (Grant No. N162504015), the China Scholarship Council (Grant No. 201706085022).

Author Contributions: Bo Zhang and Chengjun Liu conceived and designed the experiments; Guoshan Ning and Shuai Li performed the experiments; Guoshan Ning, Shuai Li and Yun Ye analyzed the data; Maofa Jiang contributed reagents/materials/analysis tools; Bo Zhang and Guoshan Ning wrote the paper.

Conflicts of Interest: The authors declare no conflict of interest.

References

1. Evans, K. The history, challenges, and new developments in the management and use of bauxite residue. *J. Sustain. Metall.* **2016**, *2*, 316–331. [[CrossRef](#)]
2. Klauber, C.; Gräfe, M.; Power, G. Bauxite residue issues: II. Options for residue utilization. *Hydrometallurgy* **2011**, *108*, 11–32. [[CrossRef](#)]
3. Borra, C.R.; Blanpian, B.; Pontikes, Y.; Binnemans, K.; Gerven, T.V. Recovery of rare earths and other valuable metals from bauxite residue (Red Mud): A Review. *J. Sustain. Metall.* **2016**, *2*, 365–386. [[CrossRef](#)]
4. Kalkan, E. Utilization of red mud as a stabilization material for the preparation of clay liners. *Eng. Geol.* **2006**, *87*, 220–229. [[CrossRef](#)]
5. Kumar, S.; Kumar, R.; Bandopadhyay, A. Innovative methodologies for the utilisation of wastes from metallurgical and allied industries. *Resour. Conserv. Recycl.* **2006**, *48*, 301–314. [[CrossRef](#)]
6. Binnemans, K.; Jones, P.T.; Blanpain, B.; Van, G.T.; Pontikes, Y. Towards zero-waste valorisation of rare-earth-containing industrial process residues: A critical review. *J. Clean. Prod.* **2015**, *99*, 17–38. [[CrossRef](#)]
7. Lopez, E.; Soto, B.; Arias, M. Adsorbent properties of red mud and its use for wastewater treatment. *Water Res.* **2008**, *32*, 1314–1322. [[CrossRef](#)]
8. Altundoğan, H.S.; Altundoğan, S.; Tümen, F.; Bildik, M. Arsenic adsorption from aqueous solutions by activated red mud. *Waste Manag.* **2002**, *22*, 357–363. [[CrossRef](#)]
9. Wang, S.; Ang, H.M.; Tade, M.O. Novel applications of red mud as coagulant, adsorbent and catalyst for environmentally benign processes. *Chemosphere* **2008**, *72*, 1621–1635. [[CrossRef](#)] [[PubMed](#)]
10. Sushil, S.; Alabdulrahman, A.M.; Balakrishnan, M.; Batra, V.S.; Blackley, R.A.; Hargreaves, J.S.J.; Monaghan, A.; Pulford, I.D.; Rico, J.L.; Zhou, W. Carbon deposition and phase transformations in red mud on exposure to methane. *J. Hazard. Mater.* **2010**, *180*, 409–418. [[CrossRef](#)] [[PubMed](#)]

11. Jayasankar, K.; Ray, P.K.; Chaubey, A.K.; Padhi, A.; Satapathy, B.K.; Mukherjee, P.S. Production of pig iron from red mud waste fines using thermal plasma technology. *Int. J. Miner. Metall. Mater.* **2012**, *19*, 679–684. [[CrossRef](#)]
12. Wang, W.; Pranolo, Y.; Cheng, C.Y. Recovery of scandium from synthetic red mud leach solutions by solvent extraction with D2EHPA. *Sep. Purif. Technol.* **2013**, *108*, 96–102. [[CrossRef](#)]
13. Qu, Y.; Lian, B. Bioleaching of rare earth and radioactive elements from red mud using penicillium tricolor RM-10. *Bioresour. Technol.* **2013**, *136*, 16–23. [[CrossRef](#)] [[PubMed](#)]
14. Smirnov, D.I.; Molchanova, T.V. The investigation of sulphuric acid sorption recovery of scandium and uranium from the red mud of alumina production. *Hydrometallurgy* **1997**, *45*, 249–259. [[CrossRef](#)]
15. Liu, Y.J.; Naidu, R. Hidden values in bauxite residue (red mud): Recovery of metals. *Waste Manag.* **2014**, *34*, 2662–2673. [[CrossRef](#)] [[PubMed](#)]
16. Lehmann, J.; Nadif, M. Interactions between metal and slag melts: Steel desulfurization. *Rev. Mineral. Geochem.* **2011**, *73*, 493–511. [[CrossRef](#)]
17. Ghost, A. *Secondary Steelmaking: Principles and Applications*; CRC Press: Boca Raton, FL, USA, 2001; pp. 187–223. ISBN 0-8493-0264-1.
18. Allibert, M.; Gaye, H.; Geiseler, J.; Janke, D.; Kowalski, M.; Lehmann, J.; Mills, K.C.; Neuschütz, D.; Parra, R.; Saint-Jours, C.; et al. *Slag Atlas*, 2nd ed.; Verlag Stahleisen GmbH: D-Düsseldorf, Germany, 1995; p. 105. ISBN 3-514-00457-9.
19. Tiwari, P.; Bandyopadhyay, D.; Ghosh, A. Kinetics of gasification of carbon and carbothermic reduction of iron oxide. *Ironmak. Steelmak.* **1992**, *19*, 464–468.
20. Wang, Q.; Yang, Z.; Tian, J.; Li, W.; Sun, J. Mechanisms of reduction in iron ore coal composite pellet. *Steel Res.* **1997**, *24*, 457–460.
21. Bale, C.W.; Chartrand, P.; Deckerov, S.A. FactSage thermochemical software and databases. *Calphad* **2002**, *26*, 189–228. [[CrossRef](#)]
22. Duffy, J.A. A review of optical basicity and its applications to oxidic systems. *Geochim. Cosmochim. Acta* **1993**, *57*, 3961–3970. [[CrossRef](#)]
23. Young, R.W.; Duffy, J.A.; Hassall, G.J.; Xu, Z. Use of optical basicity concept for determining phosphorus and sulphur slag-metal partitions. *Ironmak. Steelmak.* **1992**, *19*, 201–219.
24. Görnerup, M. Studies of Slag Metallurgy in Stainless Steelmaking. Doctor's Thesis, Royal Institute of Technology, Stockholm, Sweden, 1997.
25. Ohta, H.; Suito, H. Activities of SiO₂ and Al₂O₃ and activity coefficients of Fe_tO and MnO in CaO-SiO₂-Al₂O₃-MgO slags. *Metall. Mater. Trans. B* **1998**, *29*, 119–129. [[CrossRef](#)]
26. Zhang, G.H.; Chou, K.C.; Pal, U. Estimation of sulfide capacities of multicomponent slags using optical basicity. *ISIJ Int.* **2013**, *53*, 761–767. [[CrossRef](#)]

